2024-01

Residual mechanical properties of GGBS-FA-SF blended geopolymer concrete after exposed to elevated temperatures

Yu, M

10.1016/j.conbuildmat.2023.134378
Construction and Building Materials
Elsevier BV

Construction and Building Materials 411 (2024) 134378

Contents lists available at ScienceDirect

Construction and Building Materials

journal homepage: www.elsevier.com/locate/conbuildmat

Residual mechanical properties of GGBS-FA-SF blended geopolymer concrete after exposed to elevated temperatures

Min Yu [a,b], Tan Wang [b], Yin Chi [b], Dawang Li [a,c], Long-yuan Li [a,*], Feiyu Shi [a]

[a] School of Engineering, Computing and Mathematics, University of Plymouth, Plymouth PL4 8AA, UK
[b] School of Civil Engineering, Wuhan University, Wuhan 430072, China
[c] Guangdong Provincial Key Laboratory of Durability for Marine Civil Engineering, Shenzhen University, Shenzhen 518060, China

ARTICLE INFO

Keywords:
Geopolymer
Ground granulated blast-furnace slag
Fly ash
Steel fibre
Elevated temperature
Residual mechanical properties

ABSTRACT –

Geopolymer concrete has been increasingly used in industry. However, if the geopolymer concrete is blended using a single percussor its performance is often very limited by the properties of the percussor. Thus, it is preferable to use multiple percussors to produce geopolymer concrete. In this paper an experimental study is reported on the residual micro- and macro-mechanical properties of the steel-fibre reinforced geopolymer concrete blended by using combined percussors of ground granulated blast-furnace slag, fly ash, and salic fume. The experimental work included the examination of the effects of exposure temperature, the volume fractions of coarse aggregate and steel fibre on the compressive strength, elastic modulus, peak strain, toughness, and stress-strain constitutive relationship of the mixed geopolymer concrete, and the characterisation of the micro-structure of the materials after they were exposed to various elevated temperatures by using X-ray diffraction, scanning electron microscopy, thermal gravimetric analysis, and mercury intrusion porosimetry techniques. The experimental results showed that the residual compressive strength and residual elastic modulus decrease with the increase of exposure temperature regardless of the mix designs. The residual compressive strength of the geopolymer concrete is higher than that of the geopolymer mortar when they both are not reinforced with steel fibre. However, when they are reinforced with steel fibre the residual compressive strength of the geopolymer concrete is lower than that of the geopolymer mortar. Based on the experimentally obtained results, a temperature-dependent uniaxial stress–strain empirical equation is also proposed for the purpose of practical use.

1. Introduction

Ordinary Portland cement (OPC) concrete is widely used in the construction industry. However, the production of OPC produces a large amount of carbon dioxide emissions. Although many efforts have been made in recent years to use supplementary cementitious materials (SCMs) to reduce OPC contents used in concrete the production of OPC is predicted still to have an increasing trend until 2050 [1]. For the goal of reducing carbon footprint and reaching carbon neutrality, the binders with less carbon dioxide emissions would be the promising material for future constructions. Geopolymer concrete (GPC) was first reported in 1978 and is a relatively new type of green concrete. GPC is manufactured in alkaline environment through the geopolymerization of solid aluminosilicate-rich materials. Various industrial by-products can be used as the source materials of GPC. Examples include the ground granulated blast-furnace slag (GGBS), fly ash (FA), and metakaolin [2]. Previous studies showed that approximately 75% of carbon dioxide emissions can be reduced by using geopolymer as the binder in concrete when compared with the use of OPC [3–5]. Therefore, the development of GPC technology provides a sustainable solution to dealing with the challenge of carbon neutrality as well as reducing industrial wastes to improve our living environment. Furthermore, GPC has been also found to have very good properties in terms of the fire safety, durability, permeability, early strength, and workability [6–9]. Thus, it is expected that GPC would have large and broad applications in the construction industry in the future.

Currently, there are some technical barriers for the widespread utilization of GPC, for instance, no standard for the mix design, varying material properties due to the variation of source materials, extraordinary curing conditions required to get sufficient strength, etc. Thus, many structural members made of GPC are often precast and/or are in-situ assembled [10]. The main mechanical weakness of GPC is its volumetric instability. It was reported that there is about 2–4 times higher shrinkage in the GPC than in the OPC concrete [11,12].

* Corresponding author.

https://doi.org/10.1016/j.conbuildmat.2023.134378
Received 29 July 2023; Received in revised form 25 November 2023; Accepted 28 November 2023
Available online 6 December 2023

Practically, the addition of steel fibres in concrete can significantly reduce the shrinkage [13–15], and thus increasing the volume fraction of steel fibres in concrete can lead to a reduction in both the total and autogenous shrinkages because the bond stress between the fibres and matrix would resist the self-desiccation of the matrix. In addition, coarse aggregate can also serve as a restraint to the shrinkage of cement and mortar, and thus the shrinkage also decreases with increased coarse aggregate volume used in concrete [16–18].

FA may be the most popular precursor for producing GPC because of its availability [19–21]. Li et al. [22] and Abdulrahman et al. [23] examined the bond strength of reinforcing steel bars in FA-based GPC. Peng et al. [24] investigated the mechanical performance of FA-based GPC using machine learning technology. However, FA-based GPC often has low compressive strength if it is processed at ambient temperature condition. Therefore, most of its applications are limited to producing precast concrete members to which high temperature curing can be applied. GPC would have wider applications in situ construction as well as in precast concrete construction if they can demonstrate their good performance in ambient curing conditions. Many studies have found that the combined use of FA and GGBS has positive effects on the setting, workability, and early strength development of the GPC cured in ambient conditions [25,26].

Post-fire assessment is one of the most important parts in the life cycle design of buildings. When exposed to a fire, concrete experiences water evaporation, material decomposition, pore structure change, etc., which lead to the deterioration in material and mechanical properties. After a fire, the concrete structure needs to be scientifically evaluated before conclusions are drawn about whether it should go into rectification or demolition so that the safety and sustainable development of the structure can be guaranteed. Therefore, it is very important to scientifically evaluate the post-fire mechanical properties of concrete. The understanding of the post-fire performance of concrete materials after exposed to elevated temperatures is the basis for evaluating concrete buildings after a fire. Pervious studied have investigated the post-fire performance of different types of concrete, such as normal concrete, recycled aggregate concrete, lightweight aggregate concrete, fibre reinforced concrete, high-performance and ultra-high-performance concrete, and GPC blended with a single precursor [27–31], but very few were on GPC blended with multiple precursors, particularly when the GPC is reinforced with steel fibres.

The GPC has different hardening process from OPC concrete. The former is through the geopolymerization of geopolymer binder, whereas the latter is through the hydration of cement. This would lead to them to have different behaviour and performance when and after exposed to elevated temperatures. Furthermore, different precursors have different shrinkage and expansion behaviours, particularly when they are exposed to elevated temperatures. The combined use of different precursors could compensate and avoid the incompatible expansion and/or shrinkage between individual constituents mixed in GPC and thus reduce the damage generated during the heating and cooling processes of the concrete. In this paper, an experimental study is reported on the residual micro- and macro-mechanical properties of the steel-fibre reinforced geopolymer concrete blended by using combined percussors of GGBS, FA, silica fume (SF). The experimental work included the examination of the effects of exposure temperature, the volume fractions of coarse aggregate and steel fibre on the failure mode, compressive strength, elastic modulus, peak strain, toughness, and stress-strain constitutive relationship of the mixed GPC, and the characterisation of the micro-structure of the materials after they were exposed various elevated temperatures by using X-ray diffraction, scanning electron microscopy, thermal gravimetric analysis/derivative thermogravimetric analysis, and mercury intrusion porosimetry techniques. Based on the experimentally obtained results, a temperature-dependent uniaxial stress–strain empirical equation is also proposed for the purpose of practical use.

2. Materials and experiments

2.1. Raw materials and mix design

The raw materials used in the present experimental investigation include the three precursors (GGBS, class F FA, and SF, which were purchased from a company in Wuhan, China), alkaline solution, aggregate, and straight steel fibre, which are the same as those used in our previous study for thermal properties [32]. GGBS is a by-product from the blast-furnaces used to make iron. It is highly reactive even at ambient temperature. The use of GGBS as the precursor in GPC can improve the workability, setting time and early strength of fresh GPC and the durability of GPC in terms of the resistance to alkali silica reaction and sulphate attack. FA is also an industrial by-product produced by burning coal. There are two classes of FA, defined on the sum of total aluminium, silicon, and iron oxides in the ash. When the sum is greater than 70%, the FA is termed Class F, whereas when the sum is between 50% and 70%, the FA belongs to Class C. In general, class C FA shows poor reactivity with alkaline activators due to its low glass content and high calcium content. FA has very small particles of spherical shape which make the concrete highly dense and less permeable. SF is a by-product from the production of elemental silicon or alloys containing silicon in electric arc furnaces. It is a highly pozzolanic material that is used to enhance mechanical and durability properties of concrete. However, SF has very large surface area which reduces the workability of fresh concrete. The combination of these three materials can be more beneficial when used as a combined binder than using them individually. Table 1 lists the chemical and physical properties of GGBS, FA and SF. The mixing proportions of GGBS, FA, and SF in the present study were fixed about 7:2:1, as shown in Table 2. The microstructure of the GGBS, FA and SF was examined using SEM and is shown in Fig. 1, respectively. The alkaline solution is formed using the sodium hydroxide (95% NaOH) with density of 2.13 g/cm^3 and sodium silicate (30% SiO_2, 13.5% Na_2O) with density of 1.51 g/cm^3. The steel fibre has the length of ~12 mm and aspect ratio of 45, and nominal tensile strength of 2750 MPa. The use of steel fibres in GPC can reduce the brittleness of the GPC and improve the ductility of the concrete. The fine aggregate is the river sand with the fineness modulus of 2.7. The coarse aggregate is the crushed stone of sizes ranging from 5 mm to 25 mm. The sand-to-binder ratio used in the mix is 0.9 for all tested specimens. The volume fraction of the steel fibre in the mix is 0% or 2%. The volume fraction of the coarse aggregate in the mix is 0% or 30%.

The mix designs are labelled as '*SiiCAjj*', in which 'S' denotes the steel fibre and '*ii*' refers to its volume fraction in the mix, '*CA*' represents the coarse aggregate and '*jj*' refers to its volume fraction in the mix. The details of the mixes are summarized in Table 2. All GPC specimens (mortar and concrete with and without steel fibre) were designed to be exposed to a set of temperatures (20 ℃, 100 ℃, 300 ℃, 500 ℃, 700 ℃ and 900 ℃). In total, 24 groups of cylindrical specimens with the size of φ50 mm × 100 mm were prepared for the axial compressive tests and each group has three specimens of the same mix design that were used

Table 1
Chemical and physical properties of raw materials.

Composition	FA (wt%)	GGBS (wt%)	SF (wt%)
SiO_2	51.8	35.5	95.8
Al_2O_3	29.7	13.3	0.48
Fe_2O_3	5.03	1.20	1.47
MgO	1.05	8.60	0.48
CaO	6.70	39.5	0.32
K_2O	2.42	0.25	0.73
Na_2O	0.54	0.55	0.41
SO_3	0.90	0.20	0.21
TiO_2	1.22	0.84	–
Others	0.64	0.06	0.09
Specific surface area (m^2/kg)	450	521	23200
Specific gravity (kg/m^3)	2390	2910	2200

Table 2
Mixes of geopolymer mortar and geopolymer concrete (unit: kg/m^3).

Mix No.	GGBS	FA	SF	Fine aggregate	Water	Sodium silicate	NaOH	Steel fibre	Coarse aggregate
S0CA0	703	201	100	1105	229	254	6.77	\	\
S2CA0	689	197	98	1083	224	249	6.63	157	\
S0CA30	492	141	70	774	160	178	4.74	\	900
S2CA30	483	138	69	758	157	174	4.64	109.9	900

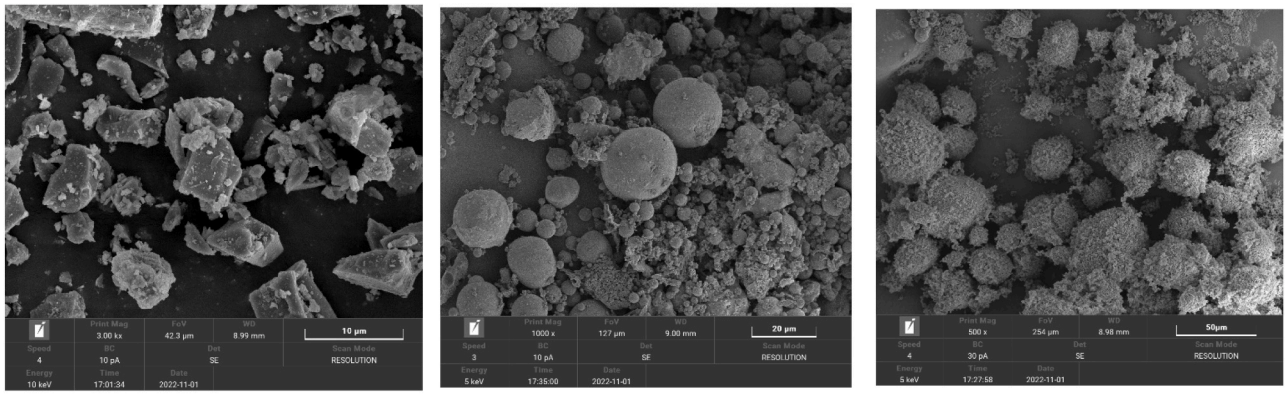

Fig. 1. SEM images of GGBS, FA and SF.

for the repeat tests. Note that in the four mix designs shown in Table 2, two (S2CA0, S0CA0) represent the geopolymer mortar (GPM) with and without steel fibre and the other two (S2CA30, S0CA30) represent the GPC with and without steel fibre.

2.2. Preparation of specimens

During the mixing process, the coarse aggregate, fine aggregate, GGBS, FA and SF were mixed first (dry mix) by a hand-held mixer for two minutes. Then the steel fibre was placed into the mixer for a further dry mixing for three minutes. NaOH was dissolved first in water for five minutes and then sodium silicate was added into the solution and stir the mixture for five more minutes to form the alkaline solution. The formed alkaline solution was then added into the mixer of solid constituents to start the wet mixing for about four minutes. After the completion of the wet mixing process, the fresh concrete was cast into the plastic moulds and vibrated for one minute. All specimens in moulds were then stored in a room of 20 °C temperature for 24 h. After the 24-hours mould curing, specimens were demoulded and then relocated to the curing room with the relative humidity of over 90% at ambient temperature for having another 28-days standard curing before they were tested.

After the curing, both end surfaces of the specimens were polished. The specimens were then heated in an electric furnace with a constant rate of 5 ℃/min until the target temperature was reached. At the target temperature, the furnace temperature was kept unchanged for about two hours to obtain a relatively uniform temperature field within the specimens. After that, the specimens were moved to the physical and mechanical testing laboratories for a natural cooling. The mechanical tests of the specimens were carried out after the specimens had cooled down to the room temperature (~ 20 °C). Fig. 2 shows the specimens at different stages during their preparation processes.

2.3. Microscopic tests

The changes of GPM and GPC specimens in material and in microstructure after they were exposed to elevated temperatures were investigated by using XRD, SEM, TGA/DTG, and MIP techniques. ESCALAB 250Xi X-Ray Photoelectron Spectroscopy with spatial resolution of 20 μm was used to examine the chemical composition of the GPM samples. The scanning angles were taken from 0° to 90°. VEGA Compact for SEM with resolution ratio of 3 nm and magnification of 2×10^6 times was used to examine the microstructure of the GPC samples. TGA2/DSC3 with the sensitivity of 0.1 μg was used to measure the change in mass with respect to the change in temperature with the heating rate of 5 ℃/min. AutoPoreV automatic MIP with the capacity of detecting pores of sizes ranging from 3 nm to 1.1 mm was used to analyse the pore size distribution and the porosity of the GPM and GPC samples. The test equipment used and the GPM and GPC samples tested are shown in Fig. 3 and Fig. 4, respectively.

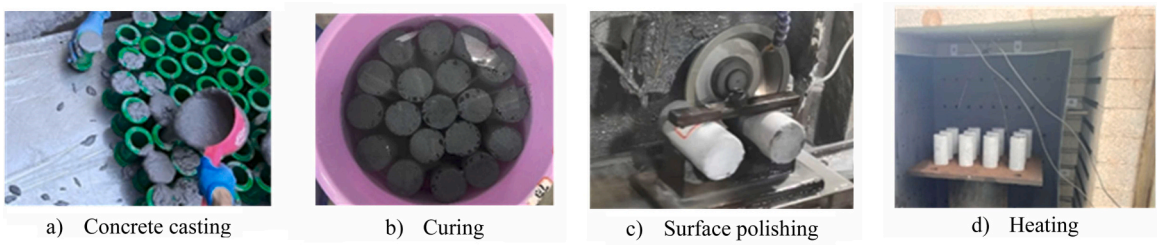

Fig. 2. Preparation of GPM and GPC specimens.

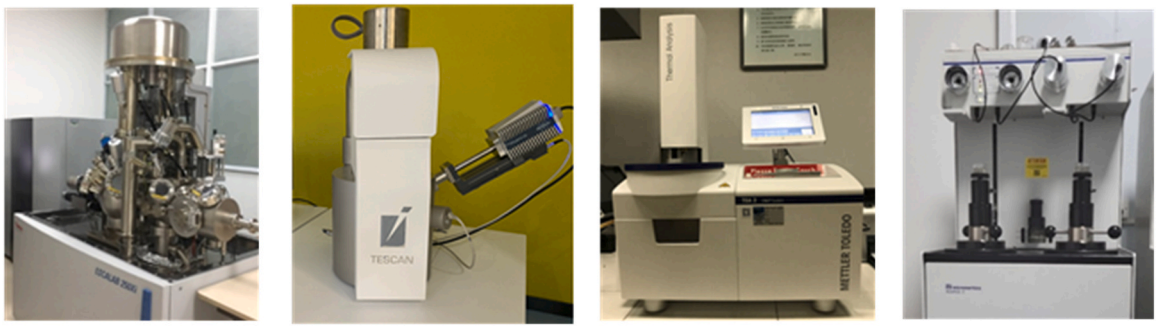

a) XRD b) VEGA Compact c) TGA2/DSC3 d) MIP

Fig. 3. Experimental equipment used for material characterisation.

a) Samples for XRD and TGA b) Samples for SEM c) Samples for MIP

Fig. 4. GPM and GPC samples used for material characterisation.

2.4. Mechanical tests

The digital image correlation (DIC) equipment with a displacement resolution of 0.001 mm was used to measure the deformation of the tested GPM and GPC specimens. As shown in Fig. 5a, lines were drawn on the side surface of the specimens before the mechanical tests so that the deformation of the specimens can be easily detected by the DIC equipment, in which the interval of the circle lines was 25 mm. The strain of the specimens was calculated based on the deformation of the two lined grids located in the middle part of the specimens, that is $\varepsilon = \Delta_{50}/50$. The axial compression tests were carried out using a servo-hydraulic material test system (MTS) with a maximum load capacity of 2500 kN (see Fig. 5b). During the test of a specimen about 30% of the peak load, which was calculated based on the compressive strength of the same mix obtained from our previous work [32], was first applied to the specimen to close the gap between the end surfaces of the specimen and the loading plates of the test machine. Then, the specimen was further loaded to 70% of its peak load with the stress rate of 0.8 MPa/s. After that, the loading control process was switched to the displacement control and the specimen was loaded at an axial displacement rate of 0.002 mm/s. The test was terminated after the load reached to its peak point and then dropped to about 20% of its peak load.

3. Microstructure analysis

3.1. X-Ray diffraction analysis

Fig. 6 shows the XRD graphs of the GPM sample after it was exposed to various elevated temperatures. It can be observed from the figure that, at the room temperature $CaMg(CO_3)_2$, $Al_6Si_2O_{13}$, C-S-H, and SiO_2 are the main components of the geopolymer paste in the GPM. No obvious change could be seen in the XRD graphs between the specimen at room temperature and that at temperature 100 ℃. As the temperature rises from 100 ℃ to 300 ℃, SiO_2 and $CaMg(CO_3)_2$ contents decrease, whereas C-S-H and $Al_6Si_2O_{13}$ are almost not changed. As the temperature rises from 300 ℃ to 500 ℃, the change in the chemical composition

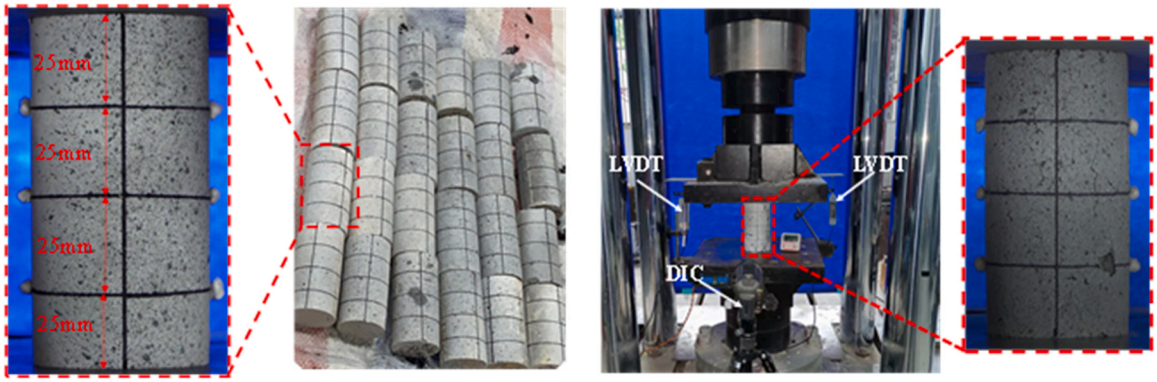

a) Specimens b) MTS servo-hydraulic dynamic loading system

Fig. 5. Experimental equipment used for mechanical tests.

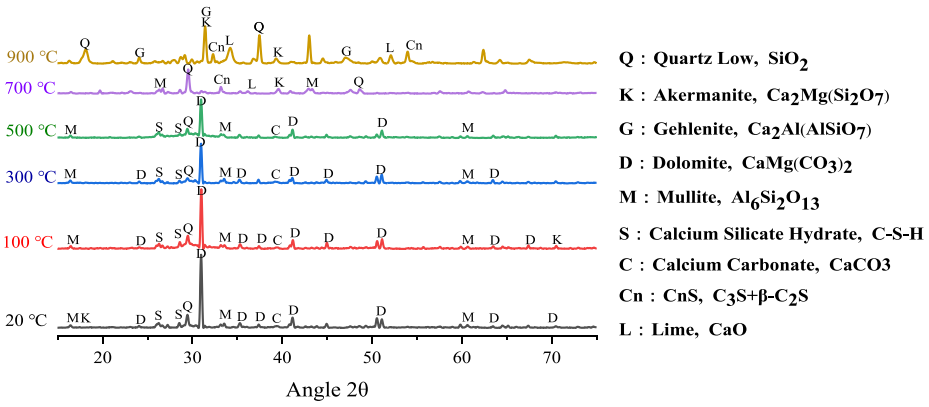

Fig. 6. XRD graphs of geopolymer mortar (S0CA0) after exposed to elevated temperatures.

of the material seems not obvious. When the temperature rises from 500 ℃ to 700 ℃, C-S-H is decomposed into β-C_2S and C_3S, which leads to the sharp decrease in the strength of C-A-S-H gel, and $CaMg(CO_3)_2$ starts to disappear. After temperature 700 °C, $Al_6Si_2O_{13}$ and $CaMg(CO_3)_2$ are decomposed almost completely, $Ca_2Mg(Si_2O_7)$ and $Ca_2Al(AlSiO_7)$ are found, in which case the C-A-S-H gel almost losses its cohesiveness.

3.2. Scanning electron microscopy analysis

Fig. 7 shows the SEM images of GPC sample after it was exposed to various elevated temperatures. It can be observed from the images that, at room temperature the matrix in GPC consists of gel, GGBS, FA and SF with dense and stable surface. The interfacial transition zone (ITZ) between the matrix and steel fibre is relatively small when the temperature is below 100 ℃. ITZ is often found in concrete, and it is the region of the cement paste and mortar around aggregate particles, which is perturbed by the presence of the aggregate. In fibre-reinforced concrete, ITZ is also found surrounding the fibre. However, as the temperature rises from 100 ℃ to 500 ℃, visible cracks can be found in the matrix which were caused by the thermal stress due to incompatible thermal deformation of different components, and the thickness of ITZ becomes large which is due to the nonuniform thermal expansion of the steel fibre in the matrix. When the temperature reaches to 700 ℃, the number of cracks in the matrix increases significantly and the surface of matrix becomes quite rough due to the decomposition of C-A-S-H gel. Meanwhile, the ITZ becomes significant larger. As the temperature reaches to 900 ℃, the matrix becomes a honeycomb-like structure.

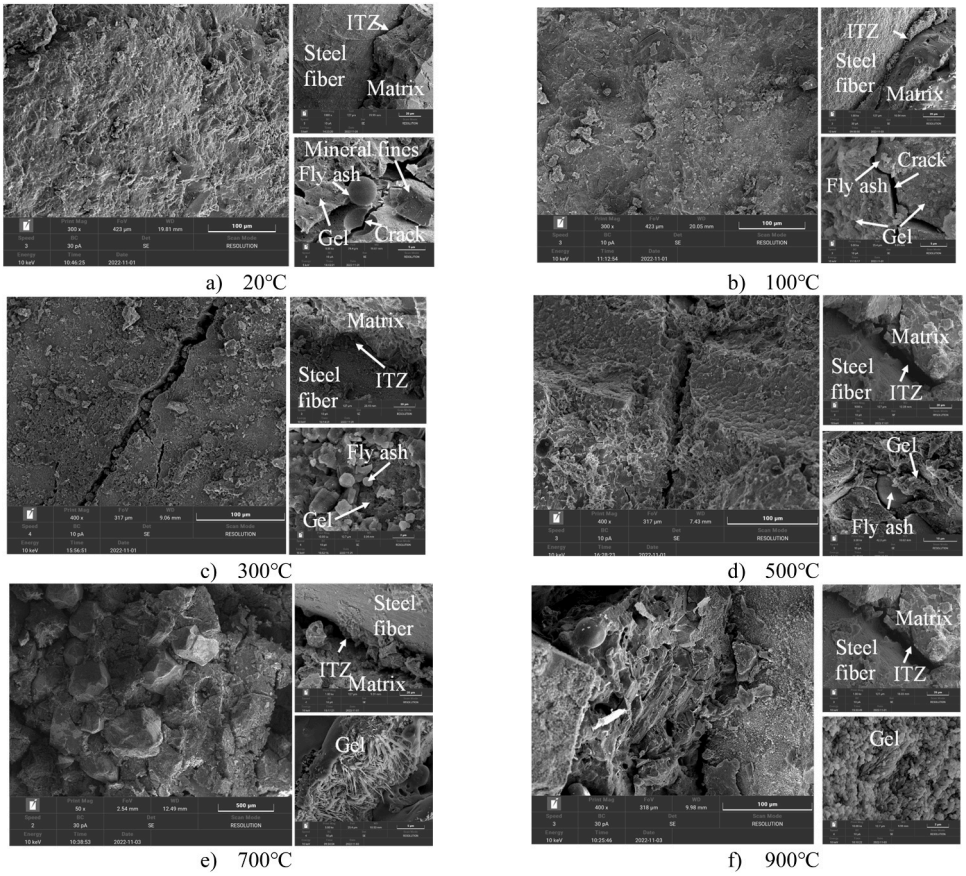

Fig. 7. SEM images of geopolymer concrete (S2CA30) after exposed to elevated temperatures.

3.3. Thermal gravimetric analysis and derivative thermogravimetric analysis

Fig. 8 shows the TGA/DTGA results of the GPM powder and the mass loss of the GPM cylindrical specimens after exposed to elevated temperatures. It can be seen from the figure that the mass loss of the powder is larger than that of the cylindrical specimen, especially for the temperature at 100 ℃. The reason for this is because not all the air inside the cylindrical specimen is released out and some of the air is trapped in the pores. With the increase of temperature, however, more pores become connected, in which case the air is easy to escape and thus the mass losses in the powder and cylindrical specimen become to be closer. It can also be found that the rate of mass loss in the powder remains almost unchanged as the temperature exceeds 700 ℃. However, the rate of mass loss in the cylindrical specimen is higher. The latter is because some parts of the cylindrical specimen become powdery.

3.4. Mercury intrusion porosimetry analysis

Fig. 9 shows the pore size distribution, porosity, and averaged pore diameter of GPM and GPC specimens at room temperature obtained from MIP measurement. It can be found from the figure that the porosity increases when the specimens were mixed with steel fibre or coarse aggregate. This increase is mainly attributed to the increase of the large pores, which is likely caused by the ITZ between the mortar and steel fibre or between the mortar and coarse aggregate. Fig. 10 shows the pore size distribution, porosity, and averaged pore diameter of GPC specimens after they were exposed to various elevated temperatures. It can be seen from the figure that, for temperature below 500 ℃ the porosity increases gradually with the increased exposure temperature. However, after the exposure temperature exceeds 500 ℃, there is a jump in both the porosity and pore sizes. The latter is mainly attributed to the microcracks generated by the thermal expansion stresses. It is these microcracks that lead to a sharp decrease in the residual strength of the concrete, which will be discussed in the Section 4 below.

4. Mechanical analysis

4.1. Failure modes of specimens

Fig. 11 shows the morphology of the GPM and GPC specimens with and without steel fibre after they were exposed to different elevated temperatures. It can be seen from the figure that, the surface colour of the specimen changed from dark to light and then back to dark while the exposure temperature increased from 20 ℃ to 900 ℃. Also, it can be observed that, when the exposure temperature reached to 500 ℃, visible cracks appeared on the specimen surface, and the cracks were more obvious for the specimens with steel fibre and/or coarse aggregate. The latter is due to the incompatibility in the thermal expansion between mortar, coarse aggregate, and steel fibre materials.

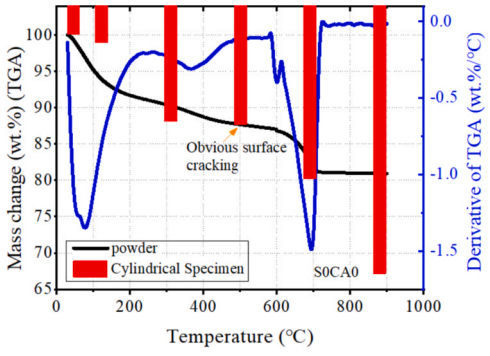

Fig. 8. Mass losses of geopolymer mortar powder (S0CA0) and geopolymer mortar cylindrical specimen (S0CA0) after exposed to elevated temperatures.

Fig. 12 shows the failure modes of the GPM and GPC specimens with and without steel fibre obtained from our compressive tests. It can be seen from the figure that the exposure temperature of the specimen has a significant effect on the compressive failure mode of the specimen, particularly when the exposure temperature is very high. For the specimens with the exposure temperature not exceeding 500 ℃, cracks can be seen on the surface of the specimens, but the specimens almost remained integrated when they failed. When the exposure temperature reached to 700 ℃, the specimens spalled off but the debris were mainly from the area surrounding a few major cracks. When the exposure temperature reached to 900 ℃, the specimens also had spalling, but the debris were in the form of powder. It can be also observed from the figure that, the failure mode of the specimens with steel fibre showed significant difference from that of specimens without steel fibre. The spalling is much less in the specimens with steel fibre than in the specimens without steel fibre, indicating that the addition of steel fibre in concrete can increase the ductility of the mixed concrete. The reason for this is partly because the randomly oriented steel fibres can absorb substantial amount of strain energy when they are pulled off from the matrix, and partly because they can prevent the widening up of concrete cracks and thus are able to maintain the specimen integration when it fails [33].

4.2. Stress-strain relationship

Fig. 13 plots the compressive stress-strain curves of the GPM and GPC specimens with and without steel fibre, obtained from the compressive tests after the specimens were exposed to various elevated temperatures. In general, the stress-strain relationship can be characterised into four different stages as shown in Fig. 14, namely, elastic stage (OA), elastoplastic stage (AB), post-peak declining stage, and failure stage. At the elastic stage, the stress increases almost linearly with the increase of strain and no obvious cracks were observed on the surface of the specimens. As the stress exceeds approximately 60% of the ultimate strength, the curve enters the elastoplastic stage, where noise was heard during the test and microcracks occurred inside the specimen. However, these microcracks were hardly visible by the naked eyes. It is noted that, for the same strain and the same temperature the stress in the specimens with steel fibres is higher than that in the specimens without steel fibres, which demonstrates that the steel fibre plays an important role in suppressing the crack development. After the stress reaches to its peak value, the curve enters the declining stage, where the cracks become visible. In this stage, the content of steel fibre has a clear effect on the bridging force. As the curve reaches to the breaking point *C* (see Fig. 14), the curve enters the failure stage. A fracture zone appears alongside the shear plane and the width of the fracture zone gradually increases.

The difference in the stress-strain curves between different exposed temperatures for each type of tested specimens can be viewed at the characteristic points of the stress-strain curves. In general, as the exposed temperature increases, the ascending part of the stress–strain curve becomes less stiff, the peak stress reduces and the corresponding peak strain increases, and the descending part of the stress-strain curve tends more flattening. The latter is more obvious for the GPC specimens reinforced with steel fibre.

4.3. Analysis of featured points and indicators

4.3.1. Compressive strength

The compressive strengths of the GPM and GPC specimens with and without steel fibre after they were exposed to various elevated temperatures, obtained from our tests are plotted in Fig. 15. It can be seen from the figure that, the overall variation trend of the compressive strength with the exposure temperature seems very similar for all the tested specimens. The slight difference in the reduction of compressive strength between the four different types of concrete tested is mainly

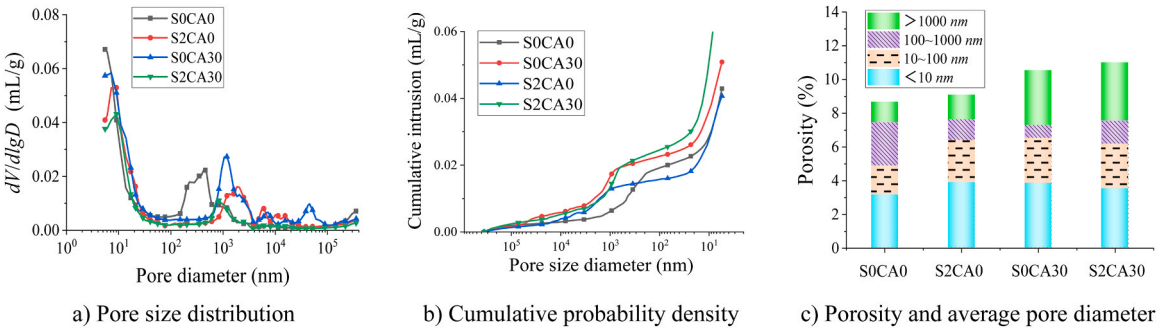

Fig. 9. Pore distribution in different mixtures at room temperature.

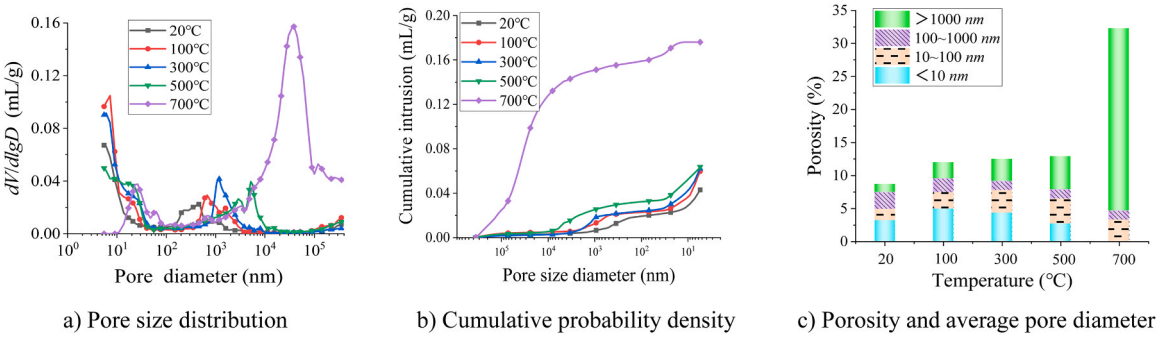

Fig. 10. Pore distribution in geopolymer concrete (S2CA30) after exposed to elevated temperatures.

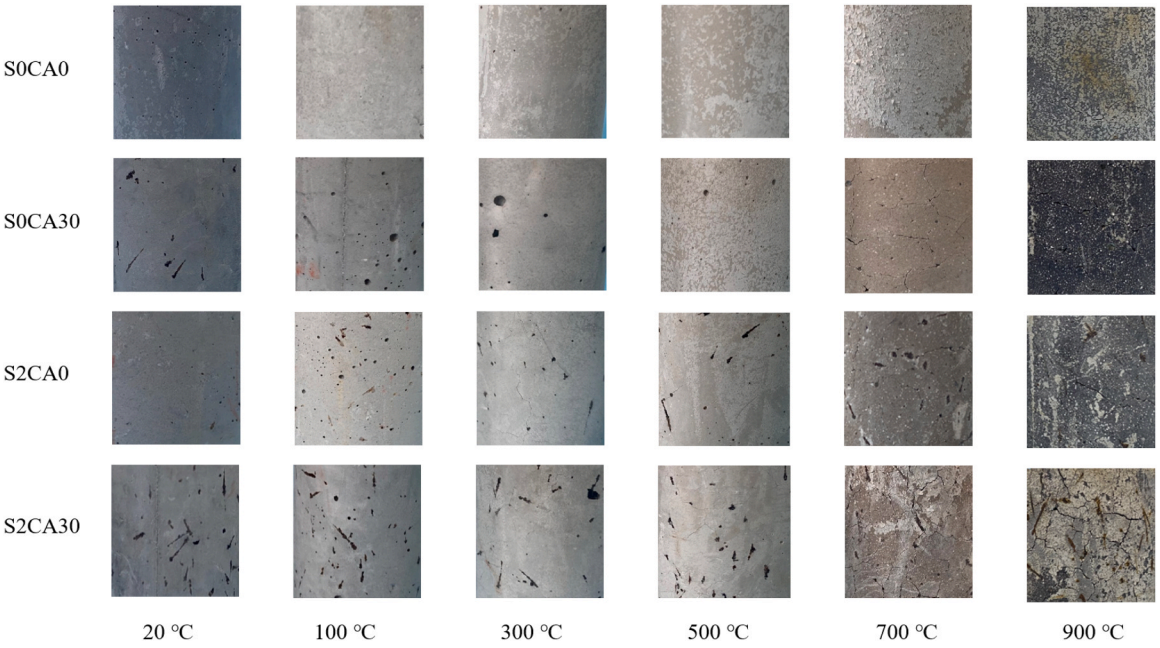

Fig. 11. Morphology of GPM sand GPC specimens after exposed to different elevated temperatures.

due to the different contributions of coarse aggregate and steel fibre mixed in the specimens [34]. For the exposure temperature between 20 ℃ and 100 ℃, all specimens have nearly 95% of their initial strengths on average. For the exposure temperatures in the range of 100–300 ℃, the compressive strength decreases sharply with increased exposure temperature. When the exposure temperature reaches to 300 ℃, the compressive strengths of GPC and GPM specimens with steel fibre reduced to about 65% of their initial strengths, whereas the compressive strengths of GPC and GPM specimens without steel fibre reduced to about 50% of their initial strengths. The reason that the compressive strength had a rapid drop when the exposure temperature is in the range of 150–300 ℃ is believed to be due to the phase transformation of calcium aluminate hydrates occurred at temperatures below 300 °C which weakened its strength [35]. For the exposure temperatures from 300 ℃ to 500 ℃, the drop in compressive strength becomes moderate for all the tested specimens. This could be attributed to the thermal incompatibility between aggregate and geopolymer matrix at high temperatures which led to the formation of internal cracks

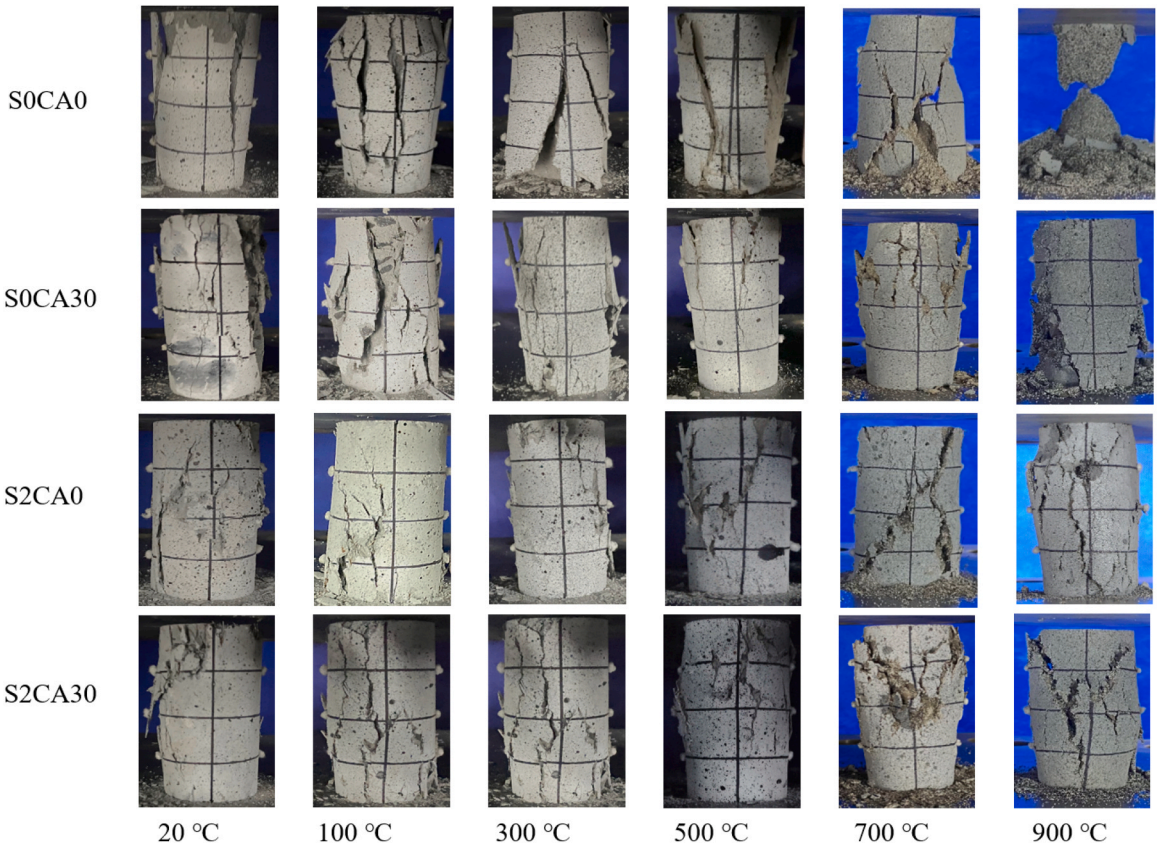

Fig. 12. Failure modes of GPM sand GPC specimens after exposed to different elevated temperatures.

and thermal stresses that weakened the concrete. When the exposure temperature increased from 500 ℃ to 700 ℃, the compressive strength decreased significantly. After they were exposed to 700 ℃, all specimens had less than 10% of their initial strengths. The reason for this is partly because the dehydration of the gels and the formation of crystals coincided with the development of larger pores and more cracks, and partly because the complete decomposition of C-A-S-H which took place around the temperature 600 °C, as both could exacerbate the mechanical degradation and volumetric disintegration [36].

Fig. 15 also shows that the compressive strength of the GPC specimen without steel fibre is higher than that of the corresponding GPM specimen without steel fibre regardless of the exposure temperature, indicating that the coarse aggregate has a positive effect on the compressive strength of GPC. Moreover, the comparison of compressive strengths between the GPM specimens with and without steel fibre or between the GPC specimens with and without steel fibre shows that the addition of steel fibre in mortar or in concrete can significantly increase the compressive strength of the mixed mortar or concrete despite the exposure temperature; this appears to be consistent with what was reported in literature [29,37]. However, it is interesting to note that the compressive strength of the steel fibre-reinforced GPC specimen is not as good as that of the steel fibre-reinforced GPM specimen for most of exposure temperatures. This is probably due to the low workability and high porosity caused by the steel fibre and coarse aggregate when they both were mixed in concrete, which produces more defects in steel fibre-reinforced GPC than in steel fibre-reinforced GPM and leads to a decrease in strength in the steel fibre-reinforced GPC. In addition, the thermal incompatibility between steel fibre and coarse aggregate around temperatures 300 °C and 500 °C may also damage the binding of steel fibre in GPC matrix and thus reduce the residual strength of the steel fibre-reinforced GPC.

The residual compressive strength of the steel fibre-reinforced OPC concrete after exposed to various elevated temperatures has been reported in literature [29,37]. The summarised results given by Wu et al. [29] (Fig. 6, page 7) showed that the relative residual compressive strength of steel fibre-reinforced OPC concrete with SCMs reduces almost linearly with the exposed temperature, and when the exposed temperature reaches to 800 °C the corresponding relative residual compressive strength is about 20~30%. This kind of reduction trend in residual compressive strength appears different from what is shown here in Fig. 15b where the sharp reduction occurs mainly in the two temperature zones. This demonstrates that the residual properties of GPM and GPC are different from that of OPC concrete after exposed to elevated temperatures.

4.3.2. *Elastic modulus*

In the present study, the elastic modulus was calculated based on the secant modulus at the 40% stress level of its peak stress. Fig. 16 plots the variation of the elastic modulus with exposure temperature for GPM and GPC specimens with and without steel fibre. It can be seen from the figure that the elastic modulus decreases sharply with the increase of exposure temperature regardless of the concrete mix design. The residual elastic modulus was about 92%, 37%, 26%, 5% and 4% of its ambient elastic modulus (20 ℃) on average after the specimen was exposed to temperature 100 ℃, 300 ℃, 500 ℃, 700 ℃ and 900 ℃, respectively. Like to the strength reduction, the elastic modulus reduction was also found to be very quick in the exposure temperature ranges from 100 ℃ to 300 ℃ and from 500 ℃ to 700 ℃. Furthermore, by comparing the results shown in Fig. 15 and Fig. 16, one can find that, for the same mix design and the same exposure temperature the reduction in elastic modulus is greater than the reduction in compressive strength. Overall, the GPC specimens have higher elastic modulus than GPM specimens regardless of the exposure temperatures, indicating that the coarse aggregate plays an important role in increasing the stiffness of

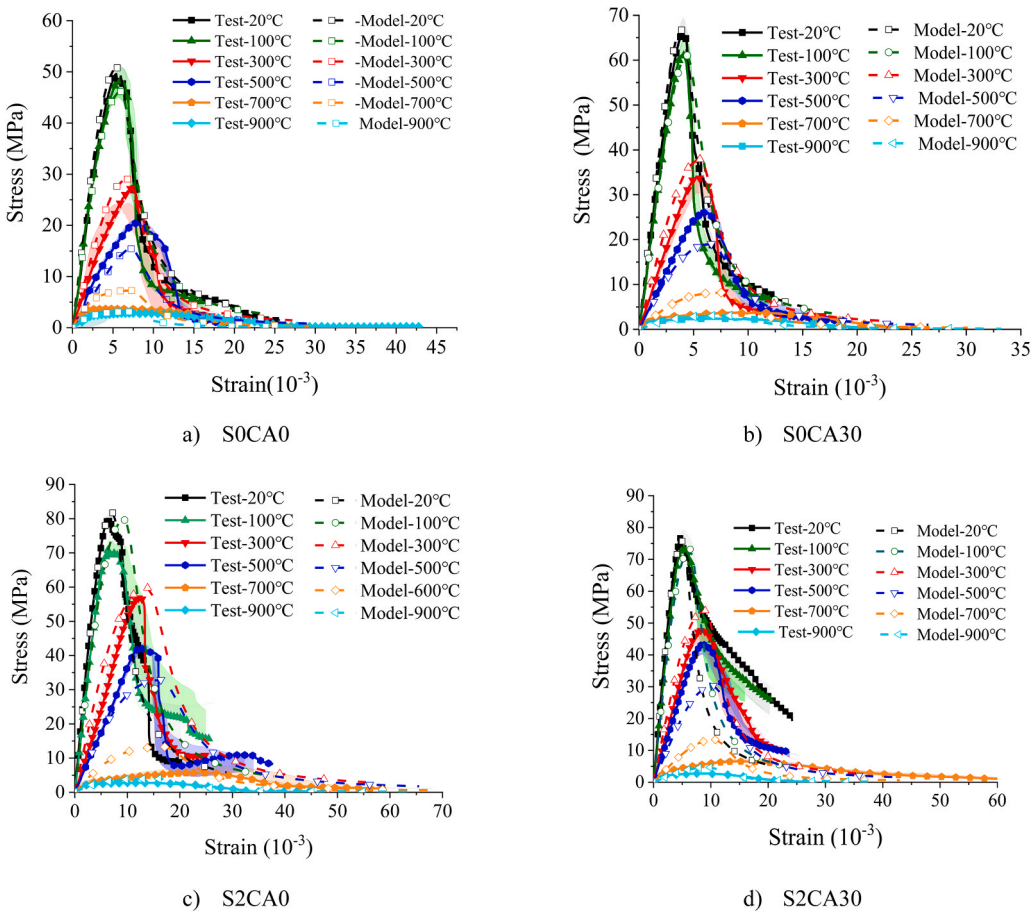

Fig. 13. Stress–strain curves of GPM and GPC specimens after exposed to different elevated temperatures (model curves will be discussed in Section 4.4).

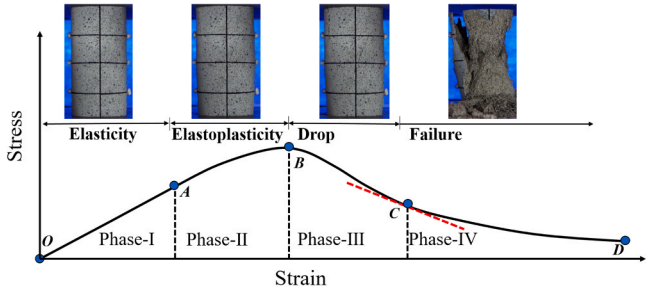

Fig. 14. Typical axial compression stress-strain curve.

concrete. The effect of steel fibre on the elastic modulus is found more remarkable in the GPM specimen when the exposure temperature is not greater than 100 °C. In contrast, its effect on the elastic modulus of GPC specimen is rather small and almost negligible.

4.3.3. Peak strain

The peak strain of a specimen refers to the strain of the specimen when the applied stress is at the peak point of the stress-strain curve, which is one of the measures reflecting the deformation capability of the concrete. Fig. 17 shows the variation of the peak strain with exposure temperature for the GPM and GPC specimens with and without steel fibre. It can be seen from the figure that, for all specimens the peak strain increases with increased exposure temperature. On average, the peak strain of the specimens tested increased by 1.01, 1.43, 1.6, 2.47 and 1.64 times after they were exposed to the temperature 100 ℃, 300 ℃, 500 ℃, 700 ℃ and 900 ℃, respectively. For the specimens with different mixes, the rate of the increase is also different. It seems that the GPM specimen without steel fibre has the lowest increase rate, followed by the GPC specimen without steel fibre. The GPM specimen with steel fibre has the largest increase rate, indicating that the addition of steel fibre in GPM or in GPC can improve the deformation capability of the mixed concrete. Also, it can be seen from the figure that, in general, GPM has higher peak strain than GPC.

4.3.4. Toughness

Toughness is referred to as the capability of the material to absorb energy and deform plastically without any fracture, which is an important parameter used for evaluating the ductility of the material. As indicated in Fig. 18, in the present study the toughness index is calculated as the ratio of the post-peak area (S_B) above the 0.3 f_c stress line to the pre-peak area (S_A) also above the 0.3 f_c stress line in the stress-strain curve where f_c is the peak stress [38]. Fig. 19 shows the variation of the toughness index of the GPM and GPC specimens with and without steel fibre with exposure temperature. It can be seen from the figure that, for all tested specimens the relative toughness index exhibits an initial decreasing trend, followed by a slight recovering for the GPM and GPC specimens with steel fibre or an increasing for the GPM and GPC specimens without steel fibre. This indicates that the effect of exposure temperature on the toughness index of GPM (or GPC) with and without steel fibre is significantly different.

4.4. Stress–strain-temperature equations of GPM and GPC after exposed to elevated temperatures

Based on the experimentally obtained stress-strain data shown in Fig. 13, we have performed a regression analysis for each type of mixed

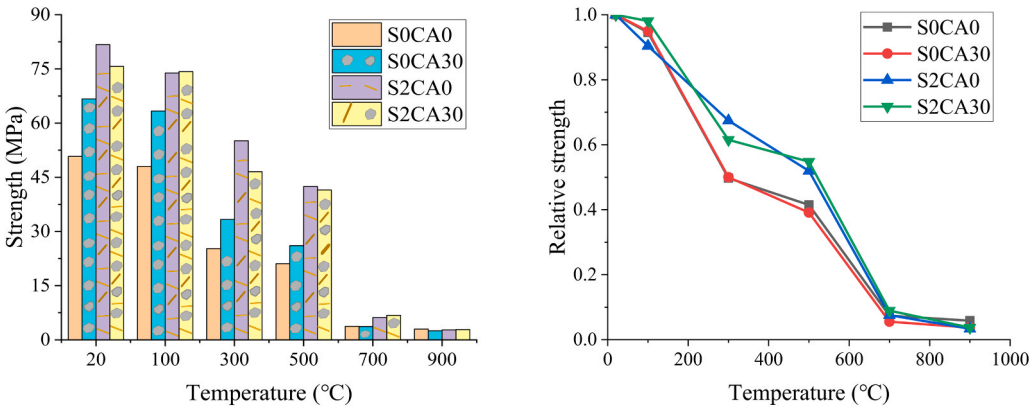

a) Compressive strength vs. temperature b) Relative Compressive strength vs. temperature

Fig. 15. Compressive strengths of GPM and GPC specimens after exposed to elevated temperatures.

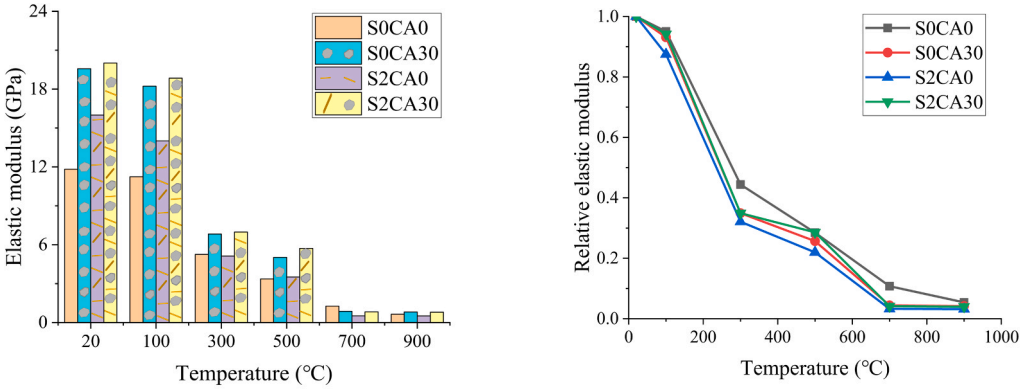

a) Elastic modulus vs. temperature b) Relative elastic modulus vs. temperature

Fig. 16. Elastic moduli of GPM and GPC specimens after exposed to elevated temperatures.

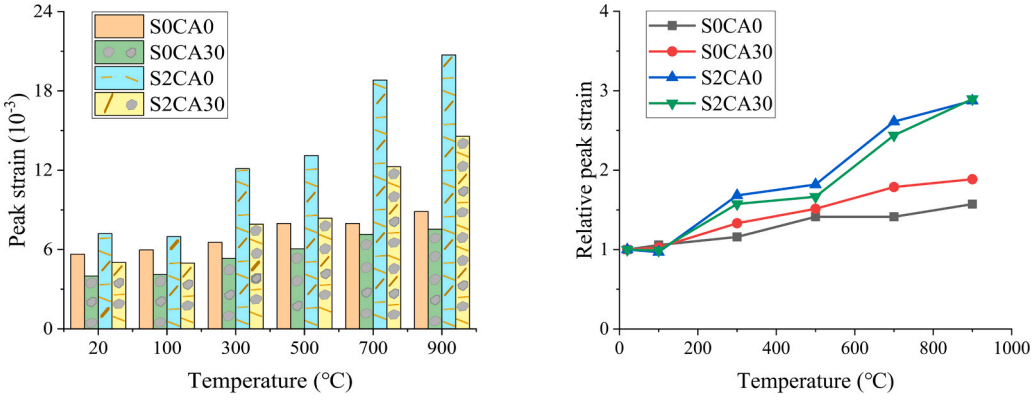

a) Peak strain vs. temperature b) Relative peak strain vs. temperature

Fig. 17. Peak strains of GPM and GPC specimens after exposed to elevated temperatures.

GPM and GPC, from which the following empirical formulas are obtained for the residual compressive strength, residual elastic modulus, peak strain, and toughness index,

$$f_{c,T} = f_{c,0} \cdot e^{-\left(a_f \cdot \frac{T-20}{1000}\right)^{b_f}} \quad (1)$$

$$\varepsilon_{p,T} = \varepsilon_{p,0}\left(a_\varepsilon\left(\frac{T-20}{1000}\right)^2 + b_\varepsilon\left(\frac{T-20}{1000}\right) + 1\right) \quad (2)$$

$$E_T = E_0 \cdot e^{-\left(\frac{T-20}{300}\right)^{b_E}} \quad (3)$$

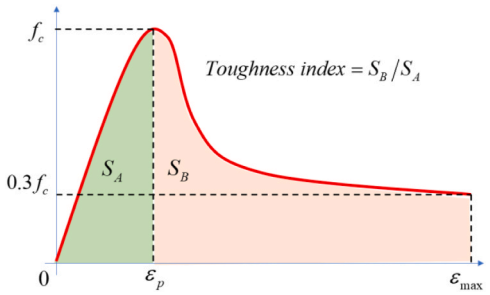

Fig. 18. Definition of toughness index for concrete materials.

$$\gamma_T = \gamma_0\left(a_\gamma\left(\frac{T-20}{1000}\right)^2 + b_\gamma\left(\frac{T-20}{1000}\right) + 1\right) \tag{4}$$

where $f_{c,0}$ and $f_{c,T}$ are the peak stresses of the specimen at ambient temperature and after it was exposed to temperature T, $\varepsilon_{p,0}$ and $\varepsilon_{p,T}$ are the peak strains of the specimen at ambient temperature and after it was exposed to temperature T, E_0 and E_T are the elastic moduli of the specimen at ambient temperature and after it was exposed to temperature T, γ_0 and γ_T are the toughness indexes of the specimen at ambient temperature and after it was exposed to temperature T, and a_f, b_f, a_ε, b_ε, b_E, a_γ, b_γ are the fitting constants, respectively. The values of these fitting constants are listed in Table 3.

To demonstrate the above proposed empirical equations, Fig. 20 shows the comparisons of the compressive strength, elastic modulus, peak strain, and toughness index results obtained from our experiments and the proposed equations. It is evident that all four parameters have very good agreement between the experimental data and calculated results.

Several analytical models have been proposed to interpret the experimental stress–strain-temperature curve [34,39,40]. Chinese Code for design of concrete structures (GB50010) also provides a stress–-strain-temperature relation expressed by Eq.(5) as follows [41–43],

$$\sigma_T = \begin{cases} \dfrac{\rho_{c,T}n}{n-1+x^n}E_T\varepsilon_T, & x \le 1 \\ \dfrac{\rho_{c,T}}{\alpha_{c,T}(x-1)^2+x}E_T\varepsilon_T, & x > 1 \end{cases}, \quad n = \frac{E_T\varepsilon_{p,T}}{E_T\varepsilon_{p,T}-f_{c,T}}, \quad \rho_{c,T} = \frac{f_{c,T}}{E_T\varepsilon_{p,T}} \tag{5}$$

where $x = \varepsilon_T/\varepsilon_{p,T}$, ε_T is the compressive strain, σ_T is the compressive stress, and $\alpha_{c,T}$ is the independent factor that controls the shape of the descending part of the stress-strain curve.In the present study, the ascending part of the stress-strain curve ($x \le 1$) given in the Code (GB50010) is adopted. However, the descending part of the stress-strain curve ($x > 1$) is obtained by using Eq.(6) for $\alpha_{c,T}$, which is obtained by the best fit of Eq.(5) to our experimental data,

$$\alpha_{c,T} = \alpha_{c,0}\left(a_\alpha\left(\frac{T-20}{1000}\right)^2 + b_\alpha\left(\frac{T-20}{1000}\right) + 1\right) \tag{6}$$

where a_α, b_α, $\alpha_{c,o}$ are the fitting constants and their values are given in Table 3. To validate the proposed model, that is Eqs.(1)–(6), the stress–strain-temperature curves calculated from the present model for each type of mixed GPM and GPC are also plotted in Fig. 13. It can be seen from the comparisons shown in the figure that, the proposed stress-strain-temperature model agrees well with the test results for both the GPM and GPC specimens with and without steel fibre.

5. Conclusions

In the present paper we have reported an experimental investigation on the micro- and macro-mechanical properties of GPM and GPC produced by using multiple precursors (GGBC, FA and SF), with and without steel fibre after they were exposed to various elevated temperatures. The work includes the material characterisation analysis using XRD, SEM, TGA/DTG and MIP techniques, and the compressive strengths and stress-strain curves of GPM and GPC specimens with and without steel fibre using standard compressive tests. Based on the obtained experimental results, an exposure temperature-dependent stress-strain constitutive equation has been also proposed to describe the effect

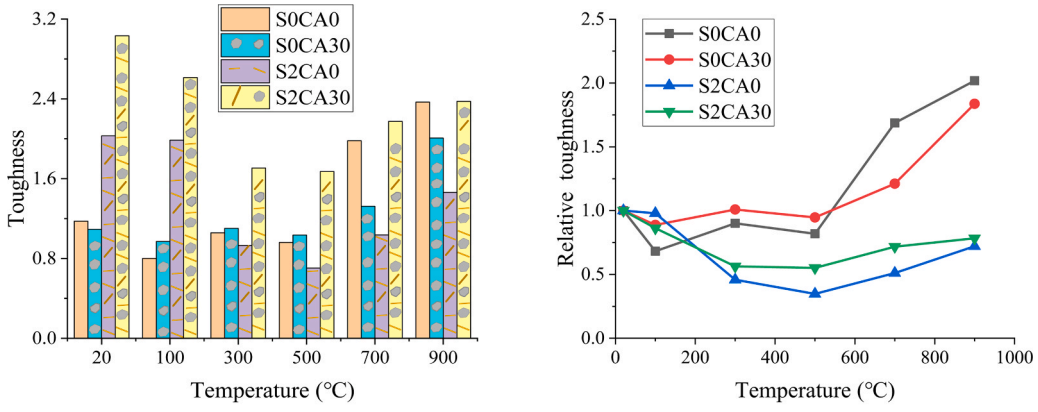

a) Toughness vs. temperature b) Relative Toughness vs. temperature

Fig. 19. Toughness of GPM and GPC specimens after exposed to elevated temperatures.

Table 3
Model paramaters used in different mixes.

	a_f	b_f	b_E	a_ε	b_ε	a_γ	b_γ	a_α	b_α	$\alpha_{c,0}$
S0CA0	2.36	1.4	1.38	-0.87	1.1	3.2	-1.54	-1.16	-0.02	7.19
S0CA30	2.43	1.48	1.17	-0.44	1.66	2.62	-1.1	-1.16	-0.02	8.89
S2CA0	2	2	1.14	-3.2	4.16	2.42	-2.43	-14.6	12.5	2.06
S2CA30	2	1.8	1.23	-2.9	3.69	1.42	-1.6	-7.7	6.9	2.13

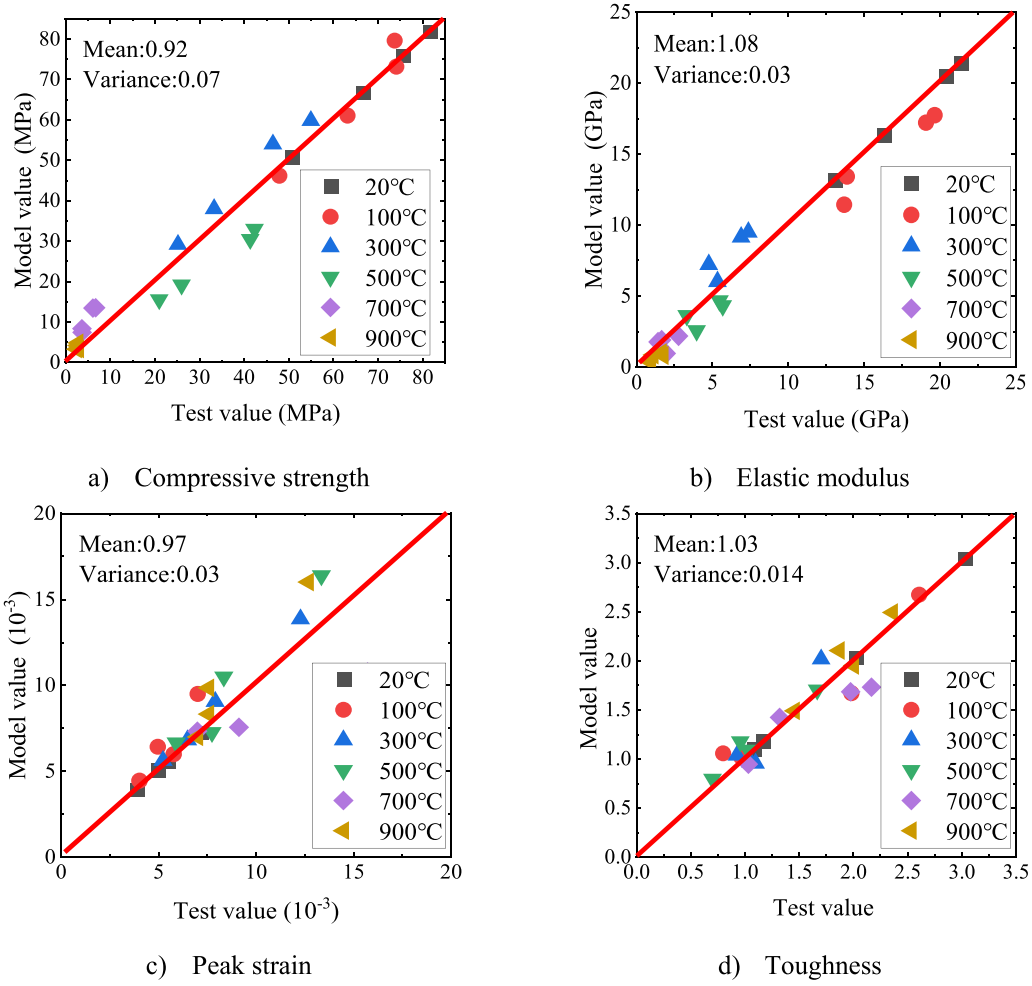

Fig. 20. Comparison between experimental results and proposed model results.

of the exposure temperature on the mechanical properties of the GPM and GPC. From the present study the following conclusions can be drawn:

1) The geopolymer products made from GGBS, FA and SF would have a phase transformation at temperatures below 300 °C, which will weaken its strength at some extent. When the exposure temperature exceeds 700 °C, the complete decomposition of C-A-S-H, the dehydration of gels, and the formation of crystals accompanying with the development of large pores and more cracks lead to a great loss in strength of the material.
2) The residual compressive strengths of GPM and GPC specimens with and without steel fibre decrease with the increased exposure temperature. The residual compressive strength of the GPM or GPC specimen with steel fibre is higher than that of the GPM or GPC specimen without steel fibre. GPC specimen has higher residual compressive strength than GPM specimen when they are not reinforced with steel fibre. However, when they are reinforced with steel fibre, the residual compressive strength of the GPM specimen is slightly higher than that of the GPC specimen.
3) The reduction of the compressive strength of the GPM and GPC specimens with and without steel fibre was found more rapid in the two exposure temperature ranges. One is between 150 ℃ and 300 ℃ where the phase transformation of calcium aluminate hydrates takes place, and the other is between 500 ℃ and 700 °C where large pores and cracks were developed due to the dehydration of the gels, the formation of crystals, and the complete decomposition of C-A-S-H.
4) In all the tested specimens, the reduction of the residual elastic modulus was found to be quicker than that of the residual compressive strength. Overall, the GPC specimens have higher residual elastic modulus than GPM specimens regardless of the exposure temperatures. The effect of steel fibre on the elastic modulus was found more remarkable in the GPM specimens than in GPC specimens.
5) For all the tested specimens the peak strain increases with increased exposure temperature, but the increase rate is different for different mixes. The GPM specimen without steel fibre has the lowest increase rate, followed by the GPC specimen without steel fibre. The GPM specimen with steel fibre has the largest increase rate, indicating that the addition of steel fibre in GPM or in GPC can improve the deformation capability of the mixed concrete.
6) The residual stress-strain constitutive equation of the GPM and GPC with and without steel fibre after they were exposed to various elevated temperatures can be described by using the stress-strain equation proposed in Chinese design code but the compressive strength, peak strain, elastic modulus, and the shape control parameter used in the equation have to be redefined and they have to be exposure temperature dependent.

CRediT authorship contribution statement

Min Yu: Writing – original draft, Validation, Supervision, Methodology, Formal analysis, Conceptualization, Discussion. **Tan Wang**: Investigation, Formal analysis, Data curation, Discussion. **Yin Chi**: Writing – review & editing, Discussion. **Dawang Li**: Conceptualization,

Supervision, Funding acquisition, Discussion. **Long-yuan Li**: Writing – review & editing, Writing – original draft, Supervision, Methodology, Funding acquisition, Conceptualization, Discussion. **Feiyu Shi**: Writing – review & editing, Discussion.

Declaration of Competing Interest

The authors declare that they have no known competing financial interests or personal relationships that could have appeared to influence the work reported in this paper.

Data Availability

No data was used for the research described in the article.

Acknowledgements

The authors would like to acknowledge the financial support received from the National Natural Science Foundation of China under grant No. 52078300 and No. 51978406, and the Marie Skłodowska-Curie Individual Fellowships (H2020-MSCA-IF-2020) under grant No. 101022142 (TemGPC).

References

[1] M.S. Imbabi, C. Carrigan, S. McKenna, Trends and developments in green cement and concrete technology, Int. J. Sustain. Built Environ. 1 (2) (2012) 194–216.
[2] A.A. Shahmansouri, H.A. Bengar, S. Ghanbari, Compressive strength prediction of eco-efficient GGBS-based geopolymer concrete using GEP method, J. Build. Eng. 31 (2020), 101326.
[3] S. Oyebisi, F. Olutoge, P. Kathirvel, I. Oyaotuderekumor, D. Lawanson, J. Nwani, A. Ede, R. Kaze, Sustainability assessment of geopolymer concrete synthesized by slag and corncob ash, Case Stud. Constr. Mater. 17 (2022), e1665.
[4] R. Robayo-Salazar, J. Mejía-Arcila, R.M. de Gutiérrez, E. Martínez, Life cycle assessment (LCA) of an alkali-activated binary concrete based on natural volcanic pozzolan: a comparative analysis to OPC concrete, Constr. Build. Mater. 176 (2018) 103–111.
[5] N. Akhtar, T. Ahmad, D. Husain, A. Majdi, M.T. Alam, N. Husain, A.K.S. Wayal, Ecological footprint and economic assessment of conventional and geopolymer concrete for sustainable construction, J. Clean. Prod. 380 (2022), 134910.
[6] Y. Yang, L. Huang, L. Xu, M. Yu, H. Ye, Y. Chi, Temperature-dependent compressive stress-strain behaviors of alkali-activated slag-based ultra-high strength concrete, Constr. Build. Mater. 357 (2022), 129250.
[7] W.E. Ooi, Y.M. Liew, C.Y. Heah, M.,M.A.B. Abdullah, L.Y. Li, Li, N. Ho, F.K. Loong, S.W. Ong, H.T. Ng, Y.S. Ng, N.A. Jaya, Comparative mechanical and microstructural properties of high calcium fly ash one-part geopolymers activated with Na2SiO3-anhydrous and NaAlO2, J. Mater. Res. Technol. 15 (2021) 3850–3866.
[8] I.H. Aziz, M.M.A.B. Abdullah, M.A.A.M. Salleh, S. Yoriya, J. Chaiprapa, C. Rojviriya, L.Y. Li, Microstructure and porosity evolution of alkali activated slag at various heating temperatures, J. Mater. Res. Technol. 9 (6) (2020) 15894–15907.
[9] R. Mohamed, R.A. Razak, M.M.A.B. Abdullah, S.Z.A. Rahim, L.Y. Li, A.V. Sandu, J. J. Wysłocki, Heat evolution of alkali-activated materials: a review on influence factors, Constr. Build. Mater. 314 (Part B) (2022), 125651.
[10] K.H. Mo, U.J. Alengaram, M.Z. Jumaat, Structural performance of reinforced geopolymer concrete members: a review, Constr. Build. Mater. 120 (2016) 251-–264.
[11] S. Hanjitsuwan, B. Injorhor, T. Phoo-ngernkham, N. Damrongwiriyanupap, L.Y. Li, P. Sukontasukkul, P. Chindaprasirt, Drying shrinkage, strength and microstructure of alkali-activated high-calcium fly ash using FGD-gypsum and dolomite as expansive additive, Cem. Concr. Compos. 114 (2020), 103760.
[12] C.D. Atiş, C. Bilim, O. Çelik, O. Karahan, Influence of activator on the strength and drying shrinkage of alkali-activated slag mortar, Constr. Build. Mater. 23 (1) (2009) 548–555.
[13] C. Fang, M. Ali, T. Xie, P. Visintin, A.H. Sheikh, The influence of steel fibre properties on the shrinkage of ultra-high performance fibre reinforced concrete, Constr. Build. Mater. 242 (2020), 117993.
[14] D. Yoo, J. Park, S. Kim, Y. Yoon, Combined effect of expansive and shrinkage-reducing admixtures on the properties of ultra high performance fiber-reinforced concrete, J. Compos. Mater. 48 (16) (2014) 1981–1991.
[15] D. Yoo, N. Banthia, Y. Yoon, Effectiveness of shrinkage-reducing admixture in reducing autogenous shrinkage stress of ultra-high-performance fiber-reinforced concrete, Cem. Concr. Compos. 64 (2015) 27–36.
[16] W. Zhu, J. Wei, F. Li, T. Zhang, Y. Chen, J. Hu, Q. Yu, Understanding restraint effect of coarse aggregate on the drying shrinkage of self-compacting concrete, Constr. Build. Mater. 114 (2016) 458–463.
[17] T.C. Hansen, K. Nielsen, Influence of aggregate properties on concrete shrinkage, J. Am. Concr. Inst. 62 (7) (1965) 783–794.
[18] A. Idiart, J. Bisschop, A. Caballero, P. Lura, A numerical and experimental study of aggregate-induced shrinkage cracking in cementitious composites, Cem. Concr. Res. 42 (2) (2012) 272–281.
[19] P. Nuaklong, P. Worawatnalunart, P. Jongvivatsakul, S. Tangaramvong, T. Pothisiri, Pre- and post-fire mechanical performances of high calcium fly ash geopolymer concrete containing granite waste, J. Build. Eng. 44 (2021) 103265..
[20] K. Pasupathy, D.S. Cheema, J. Sanjayan, Durability performance of fly ash-based geopolymer concrete buried in saline environment for 10 years, Constr. Build. Mater. 281 (2021), 122596.
[21] M.T. Ghafoor, Q.S. Khan, A.U. Qazi, M.N. Sheikh, M.N.S. Hadi, Influence of alkaline activators on the mechanical properties of fly ash based geopolymer concrete cured at ambient temperature, Constr. Build. Mater. 273 (2021), 121752.
[22] Y. Li, J. Shen, H. Lin, H. Li, J. Lv, S. Feng, J. Ci, The data-driven research on bond strength between fly ash-based geopolymer concrete and reinforcing bars, Constr. Build. Mater. 357 (2022), 129384.
[23] H. Abdulrahman, R. Muhamad, P. Visintin, A.A. Shukri, Mechanical properties and bond stress-slip behaviour of fly ash geopolymer concrete, Constr. Build. Mater. 327 (2022), 126909.
[24] Y. Peng, C. Unluer, Analyzing the mechanical performance of fly ash-based geopolymer concrete with different machine learning techniques, Constr. Build. Mater. 316 (2022), 125785.
[25] A. Bouaissi, L.Y. Li, M.M.A.B. Abdullah, Q.B. Bui, Mechanical properties and microstructure analysis of FA-GGBS-HMNS based geopolymer concrete, Constr. Build. Mater. 210 (2019) 198–209.
[26] P. Nath, P.K. Sarker, Effect of GGBFS on setting, workability and early strength properties of fly ash geopolymer concrete cured in ambient condition, Constr. Build. Mater. 66 (2014) 163–171.
[27] M. Malik, S.K. Bhattacharyya, S.V. Barai, Thermal and mechanical properties of concrete and its constituents at elevated temperatures: a review, Constr. Build. Mater. 270 (2021), 121398.
[28] B. Fernandes, H. Carre, J. Mindeguia, C. Perlot, C.L. Borderie, Effect of elevated temperatures on concrete made with recycled concrete aggregates - an overview, J. Build. Eng. 44 (2021), 103235.
[29] H. Wu, X. Lin, A. Zhou, A review of mechanical properties of fibre reinforced concrete at elevated temperatures, Cem. Concr. Res. 135 (2020) 106117..
[30] O.E. Babalola, P.O. Awoyera, D.H. Le, L.M.B. Romero, A review of residual strength properties of normal and high strength concrete exposed to elevated temperatures: impact of materials modification on behaviour of concrete composite, Constr. Build. Mater. 296 (2021), 123448.
[31] Y. Zhu, H. Hussein, A. Kumar, G. Chen, A review: material and structural properties of UHPC at elevated temperatures or fire conditions, Cem. Concr. Compos. 123 (2021), 104212.
[32] M. Yu, H. Lin, T. Wang, F. Shi, D.W. Li, Y. Chi, L.Y. Li, Experimental and numerical investigation on thermal properties of alkali-activated concrete at elevated temperatures, J. Build. Eng. 74 (2023), 106924.
[33] A.L. Hoang, E. Fehling, Influence of steel fiber content and aspect ratio on the uniaxial tensile and compressive behavior of ultra high performance concrete, Constr. Build. Mater. 153 (2017) 790–806.
[34] J.A. Purkiss, L.Y. Li. Fire Safety Engineering, Design of Structures, third ed., CRC Press, Oxford, 2013.
[35] R. Cai, H. Ye, Clinkerless ultra-high strength concrete based on alkali-activated slag at high temperatures, Cem. Concr. Res. 145 (2021), 106465.
[36] N.K. Lee, K.T. Koh, G.H. An, G.S. Ryu, Influence of binder composition on the gel structure in alkali activated fly ash/slag pastes exposed to elevated temperatures, Ceram. Int. 43 (2) (2017) 2471–2480.
[37] Q. Ma, R. Guo, Z. Zhao, Z. Lin, K. He, Mechanical properties of concrete at high temperature—a review, Constr. Build. Mater. 93 (2015) 371–383.
[38] J. Zhou, J. Pan, C.K.Y. Leung, Mechanical behavior of fiber-reinforced engineered cementitious composites in uniaxial compression, J. Mater. Civ. Eng. 27 (1) (2015), 000103.
[39] M.A. Mansur, M.S. Chin, T.H. Wee, Stress-strain relationship of high-strength fiber concrete in compression, J. Mater. Civ. Eng. 11 (1) (1999) 21–29.
[40] Y.F. Chang, Y.H. Chen, M.S. Sheu, G.C. Yao, Residual stress–strain relationship for concrete after exposure to high temperatures, Cem. Concr. Res. 36 (10) (2006) 1999–2005.
[41] H. Zhao, F. Liu, H. Yang, Residual compressive response of concrete produced with both coarse and fine recycled concrete aggregates after thermal exposure, Constr. Build. Mater. 244 (2020), 118397.
[42] Y. Tang, J. Xiao, H. Zhang, Z. Duan, B. Xia, Mechanical properties and uniaxial compressive stress-strain behavior of fully recycled aggregate concrete, Constr. Build. Mater. 323 (2022), 126546.
[43] T. Wang, M. Yu, W. Shan, L. Xu, S.S. Cheng, L.Y. Li, Post-fire compressive stress–strain behaviour of steel fibre reinforced recycled aggregate concrete, Compos. Struct. 309 (2023) 116735..